Fusion Engineering and Design 231 (2026) 115955

Contents lists available at ScienceDirect

Fusion Engineering and Design

journal homepage: www.elsevier.com/locate/fusengdes

Neutron detector calibration for the KATANA facility: Experimental and computational validation of water activation neutron emission ☆

Julijan Peric [a,b,*], Domen Kotnik [a], Domen Govekar [a,b], Luka Snoj [a,b], Zdenek Vykydal [c], Marco De Pietri [d], Vladimir Radulović [a,b]

[a] Reactor Physics Department, "Jožef Stefan" Institute, Jamova cesta 39, Ljubljana, 1000, Slovenia
[b] Faculty of Mathematics and Physics, University of Ljubljana, Jadranska ulica 19, Ljubljana, 1000, Slovenia
[c] Czech Metrology Institute, Okruzni 31, Brno, 638 00, Czech Republic
[d] MIT, Plasma Science and Fusion Center (PSFC), 77 Massachusetts Avenue, Cambridge, 02139, United States

ARTICLE INFO

Keywords:
Water activation
JSI
KATANA
Neutron
Calibration
ITER

ABSTRACT

KATANA is a water activation facility located in the TRIGA Mark II reactor of the Jožef Stefan Institute in Ljubljana, Slovenia. Since its commissioning it has contributed to a better understanding of water activation processes and their modelling, which is important in the context of the future operation of the ITER tokamak. The facility is designed to provide a flexible, benchmark-quality environment for the validation of computational tools for the activation of water. It will also support shielding experiments, in particular for ITER-relevant materials, and serve as a stable source of high-energy gamma rays and neutrons. This paper presents the calibration of ^{3}He and BF_3 neutron detectors used to measure neutron emission from the decay of ^{17}N. The calibration was performed at the Czech Metrology Institute using a well-characterised graphite-moderated thermal neutron reference field. The calibrated acquisition system is then used in conjunction with Monte Carlo particle transport simulations to obtain the total neutron emission within the measurement volume of the KATANA water activation facility. The results form a basis for the determination of the integral cross section of the ^{17}O(n,p)^{17}N reaction, a nuclear reaction that is still insufficiently described in the literature.

1. Introduction

Water is widely used as a coolant in nuclear fission reactors both power and research ones, and is also expected to be used in future fusion reactors. The most relevant nuclear reactions involved in water activation are ^{16}O(n,p)^{16}N, ^{17}O(n,p)^{17}N, and ^{18}O(n,γ)^{19}O, with the reaction on ^{16}O being the most extensively studied due to its high natural abundance (99.7%) and significant activation cross-section [1]. Among the activation products, ^{17}N, produced via the ^{17}O(n,p)^{17}N reaction, plays a particularly important role in fusion-oriented applications because of its short half-life (4.17 s) and emission of high-energy neutrons in the 0.38 MeV–1.7 MeV range [2]. As this reaction requires incident neutron energies above 9 MeV, its occurrence is enhanced in neutron fields with D-T fusion spectra [3].

KATANA [4] is a water activation facility located at the Jožef Stefan Institute TRIGA Mark II (JSI TRIGA) reactor in Ljubljana, Slovenia [5]. The facility is built to address water activation challenges in future water-cooled fusion machines, such as the ITER tokamak [6,7]. Since its commissioning at the end of 2023, it has been used to successfully complete several experimental campaigns that have contributed to a better understanding of water activation processes and their modelling.

The KATANA water activation facility is built as a closed-loop system extending from the reactor core to the exterior of an irradiation port. The water circulates and becomes activated in close proximity to the reactor core. Outside the biological shield, water activation is measured in a snail- shaped volume and then returned to the irradiation part via a pump. The irradiation field around the KATANA water activation loop and the future ITER cooling circuit have the same two contributions from neutrons and gamma rays; only the intensity differs. However, because the transport equation is linear, the KATANA lower water activation intensity is also relevant for higher intensity scenarios in ITER [4,8].

The ultimate goal of the KATANA facility is to enable benchmark-quality neutron activation and dosimetry experiments, providing reliable experimental data for validating state-of-the-art computational tools used in nuclear fusion research. The development and commissioning of the facility were driven by the objective to establish a

☆ This article is part of a Special issue entitled: 'ISFNT-16' published in Fusion Engineering and Design.

* Corresponding author at: Reactor Physics Department, "Jožef Stefan" Institute, Jamova cesta 39, Ljubljana, 1000, Slovenia.
E-mail address: julijan.peric@ijs.si (J. Peric).

https://doi.org/10.1016/j.fusengdes.2026.115955
Received 25 January 2026; Received in revised form 9 July 2026; Accepted 13 July 2026
Available online 21 July 2026

Table 1
Activation products of water [2].

Reaction	$^{*}t_{1/2}$	Major decay products	Threshold energy	Natural abundance
^{16}O(n, p)^{16}N	7.13 s	γ: 6.13 MeV (67%) γ: 7.12 MeV (5%) **n: 0.38 MeV (35%)**	≈ 10 MeV	99.76%
^{17}O(n, p)^{17}N	**4.17 s**	**n: 1.17 MeV (53%)** **n: 1.70 MeV (7%)**	≈ 9 MeV	**0.04%**
^{18}O(n, γ)^{19}O	26.9 s	γ: 0.20 MeV (96%) γ: 1.36 MeV (50%)	<1 eV	0.2%

controlled and well-characterised irradiation environment suitable for high-precision measurements. In the current phase, attention is focused on characterising the working parameters and radiation fields, which is a prerequisite for the quantitative measurements at the facility to support modelling and code validation.

Particular emphasis is placed on validating newly developed computational tools for simulating the ITER cooling circuit, where accurate knowledge of neutron transport and activation phenomena is essential for design optimisation and safety assessment. The first step towards this goal is the experimental determination and modelling of the neutron field around the KATANA measurement volume. This includes measuring neutron flux, assessing neutron spectrum and spatial distributions, and comparing results with those obtained from Monte Carlo simulations.

This work reports the comprehensive characterisation of the neutron field surrounding the KATANA facility, detailing the experimental setup, measurement techniques, data analysis procedures, and computational methodologies used. The results provide the foundation for subsequent benchmarking studies and ensure the facility can be confidently used for ITER-relevant irradiation campaigns, detector calibration, and nuclear data validation. This study represents a significant step towards integrating KATANA as a reference facility for fusion-oriented neutron metrology and computational validation.

2. Water activation

The most important nuclear reactions involved in the process of water activation are summarised in Table 1. This table contains data on the nuclear reactions, including the half-life in seconds, the most important decay products, their energies in MeV and their respective branching ratios in percent (in brackets). It also contains information on the threshold energy of the reaction in MeV and the natural isotopic abundance of the parent nuclides in percent. The radioactivity of the activated water consists mainly of high-energy gamma rays and neutrons with half-lives of 7.13 s for ^{16}N, 4.17 s for ^{17}N and 26.9 s for ^{19}O. Consequently, the activated water serves as a time-dependent radiation source, emitting radiation during and shortly after reactor operation. In water activation, the reaction with ^{16}O has been the most studied due to its high natural occurrence (99.7%). In addition, the ^{16}O(n,p)^{16}N reaction has a significant activation cross-section, indicating a higher probability of interaction with neutrons compared to other oxygen isotope reactions.

This article focuses on ^{17}O due to its emission of high-energy neutrons. This is particularly important in fusion applications where the neutron spectrum is of higher energies compared to the fission spectrum, leading to a higher degree of activation. Neutrons with energies above 9 MeV are required for the ^{17}O(n, p)^{17}N reaction. The processes produce the radioisotope ^{17}N, which leads to a sequence of radioactive decay, releasing high-energy neutrons.

2.1. KATANA water activation facility

The facility provides a controlled source of high-energy γ- rays in the range 6 MeV - 7 MeV and neutrons in the range 0.4 MeV - 1.7 MeV. It was developed to enable experimental investigations of water activation phenomena and is designed for flexibility, allowing applications such as calibration of radiation detectors and dosimeters, shielding studies, validation of simulation tools for fusion cooling systems, and measurements of integral cross sections [4,8,9]. The facility consists of a closed water activation loop divided into three main components: the inner section, the outer section, and the control panel. The inner and outer sections are shown schematically in Fig. 1.

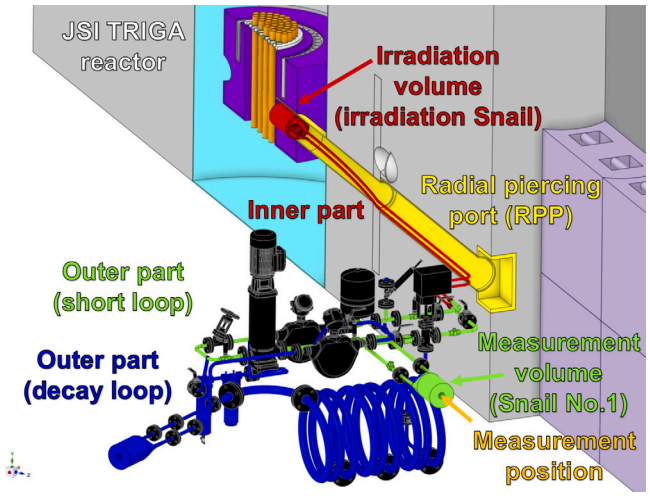

Fig. 1. Schematic representation of the KATANA water activation loop.

The inner section is installed in the Radial Piercing Port (RPP) of the JSI TRIGA reactor, where neutron interactions produce short-lived radioisotopes in the water. The activated water then circulates through pipes to the outer section, located inside the concrete shielding adjacent to the RPP. This outer section comprises two circuits connected by a three-way valve: a short loop and a longer delay loop. For the experiments described in this work, only the short loop was used, as the radionuclide of interest (^{17}N) has a short half-life. The activated water is continuously monitored in the measurement volume before being recirculated through the pump into the inner section. The system is operated and controlled remotely from the control panel located behind the concrete shielding [4].

The measurement volume, known as Snail No. 1, is named for the distinctive snail- like geometry of its internal flow path. It has a tubular configuration with internal baffles that guide the flow of activated water along a controlled trajectory. This design ensures optimised residence times within the irradiation zone, maximising the achievable dose rates in the experimental area. The external and internal geometry of Snail No. 1 was designed to replicate the shape of the inner irradiation Snail (shown in red in Fig. 1), with its overall form based on the RPP geometry of the JSI TRIGA reactor. This correspondence ensures that the flow conditions within Snail No. 1 are representative of those in the irradiation Snail.

The Snail No. 1 was fabricated using additive manufacturing techniques, employing an aluminium-based 3D printing alloy powder to achieve the required mechanical strength, geometric precision, and corrosion resistance. The use of 3D printing technology enabled the creation of internal flow structures that would be difficult or impossible to produce using conventional machining or casting methods. This approach provided design flexibility and allowed the integration of performance optimised geometrical features directly into the component.

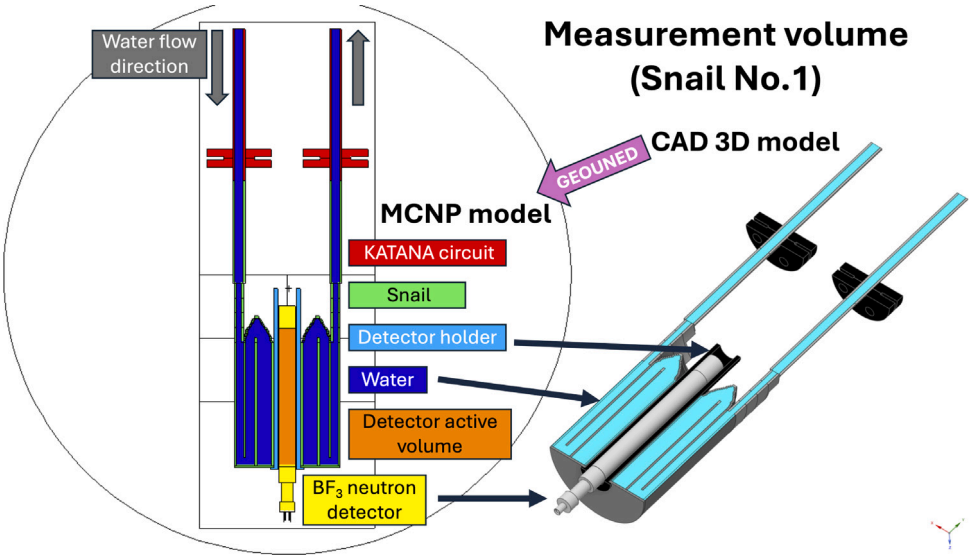

Fig. 2. XY cross-section of Snail No. 1 in the MCNP model (left) and the 3D CAD model (right). The MCNP model in the right part of the schematic shows the configuration and water flow direction. The colour coding indicates the material composition of the main components: the KATANA water circuit (red — aluminium), Snail No. 1 structure (green — 3D printable aluminium), detector holder (light blue — polyethylene), water (dark blue — water), BF_3 gas (orange), and BF_3 neutron detector body (yellow — stainless steel).

2.2. KATANA computational model

A computational model of the KATANA facility was created using the Monte Carlo N-Particle (MCNP) code [10] in order to support experimental characterisation and the determination of radiation field within the measurement volume. The model was developed based on the CAD model of the Snail No. 1. assembly, by simplification and conversion into constructive solid geometry (CSG) using the GEOUNED tool [11]. The resulting model preserves the key structural and material features relevant to neutron transport and activation. Fig. 2 presents the MCNP geometry in the XY plane at the height of the Snail centre, including the position of the BF_3 detector used for neutron field characterisation. The colour coding in the figure indicates the material composition of the components.

The neutron source in the simulation corresponds to the decay of ^{17}N isotopes produced by oxygen activation in the circulating water. The source is distributed uniformly within the water volume in Snail No. 1, with a discrete energy distribution of 0.38 MeV, 1.17 MeV, and 1.70 MeV [10].

3. Neutron detector efficiency calibration

Efficiency calibration of ^3He and BF_3 proportional counters is typically carried out in a accurately characterised neutron field in terms of neutron energy spectrum and fluence rate. Under these conditions calibration factors can be reliably determined by comparison with reference instruments or evaluated neutron flux standards [12,13].

However, when these detectors are used to measure neutron fields generated by water activation, they are exposed to a mixed neutron and gamma field, as well as a higher-energy neutron spectrum extending up to about 1.7 MeV. In this range, both detectors exhibit energy-dependent response variations due to reduced capture cross-sections and increased contributions from wall and scattering effects. Consequently, direct calibration in a high-energy neutron field is challenging because of flux gradients, uncertain spectral composition, and the lack of reference fields. Therefore, calibration in a well-defined thermal field provides a reproducible baseline, while the detector response in the activation field must be corrected using Monte Carlo simulations.

3.1. CMI national standard of thermal neutron fluence rate

The Czech Metrology Institute (CMI) is the national reference for thermal neutron fluence rate using a dedicated graphite pile facility in Prague, which provides stable and reproducible conditions for calibrations and comparisons of neutron-sensitive instruments presented in Fig. 3. The moderator assembly denoted with orange has external dimensions of approximately 1.95 m × 1.95 m × 2.0 m and incorporates a central measurement channel marked with purple 0.40 m×0.40 m, depth ≈ 1.3 m, equipped with a precision calibration bench for reproducible detector positioning denoted in blue. Six symmetrically arranged lateral openings at a radius of 80 cm accommodate sealed Pu–Be and/or Am–Be sources to generate the moderated neutron field [14–16].

The reference thermal fluence rate is established by activation of high-purity gold foils (8 mm diameter, 0.1 mm thickness) following IAEA TRS 107 procedures [17], with activities determined on a calibrated HPGe spectrometer to approximately 1% relative uncertainty. Active mapping of the field used a small cylindrical ^3He proportional counter and a Timepix silicon pixel detector with a ^{10}B converter; both systems are cross-calibrated to the activation results to yield absolute fluence rates and spatial profiles [14,18,19].

At the geometric centre of the cavity with the six neutron sources setup, the thermal neutron flux is $(1.97 \pm 0.01) \times 10^4$ cm^{-2} s^{-1}, and the cadmium ratio is $R_{Cd} \approx 35.5$ for the Au-197(n, γ) reaction, indicating low epithermal contamination in the moderated spectrum. The cadmium ratio, R_{Cd}, is defined as the ratio between the activity of a bare activation foil and that of the same foil irradiated under a cadmium cover, measured under identical irradiation and counting conditions. Monte Carlo transport calculations (MCNPX 2.7E), validated against measurements, show that the ± 5% homogeneity criterion is satisfied within a cylindrical volume of approximately 40 cm in diameter centred on the channel axis, enabling calibrations under well-defined reference conditions suitable for dissemination of traceability to end users [15].

The neutron energy spectrum inside the central measurement channel of the CMI graphite pile is characterised by a Maxwellian-like thermal distribution peaking near $E \approx 25$ meV, with a negligible epithermal tail above 0.5 eV. Fig. 4 presents the lethargy spectrum evaluated 20 cm inside the measurement cavity, illustrating the high degree of moderation and spectral stability of the reference field [15].

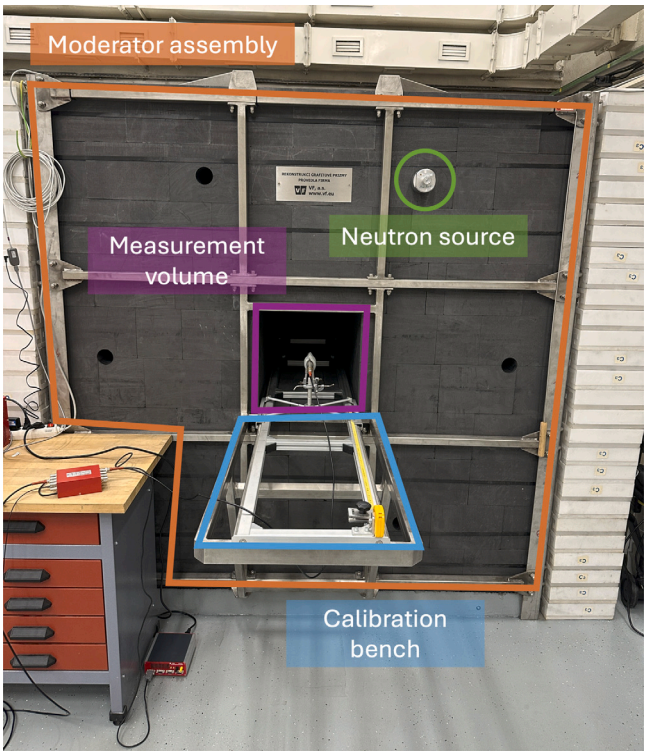

Fig. 3. CMI neutron fluence standard facility.

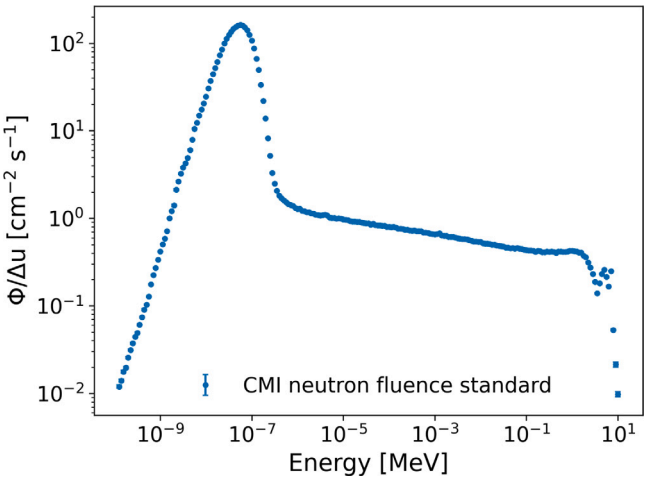

Fig. 4. CMI neutron fluence standard lethargy spectrum at 20 cm within the measurement cavity.

3.2. Calibration experiments

Calibration measurements of the ^{3}He (LND 25371) and BF_3 (LND 202) proportional counters were performed at the CMI neutron fluence standard facility on 13 May 2025, using the reference thermal field described in Section 3.1. The detectors were mounted on the precision translation bench within the central graphite channel shown in Fig. 5, allowing reproducible positioning with an accuracy of 1 mm. Each detector was connected to a CAEN A1422 preamplifier and a CAEN V1782 digital Multi Channel Analyser for signal acquisition (DAQ).

The axial neutron detector signal measured along the central channel of the CMI standard thermal neutron field is shown in Fig. 6. The experimental results obtained with the ^{3}He and BF_3 proportional counters are shown as orange and green markers, respectively, including

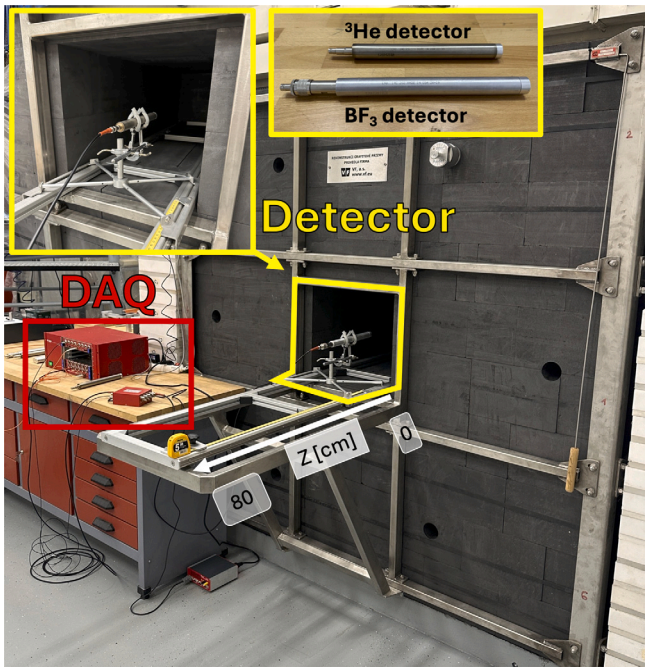

Fig. 5. Experimental setup for neutron detector calibration at the CMI neutron fluence standard facility. Measurements were conducted on 13 May 2025 under reference thermal neutron field conditions with the neutron source (Am-Be #2) in the top right position.

statistical uncertainties. The response of the ^{3}He detector is consistently higher than that of the BF_3 detector, which can be attributed to the higher thermal neutron capture cross-section and detection efficiency of ^{3}He. The blue curve represents the reference flux profile calculated using the validated MCNP model of the facility, which forms the basis of the CMI neutron fluence standard [15].

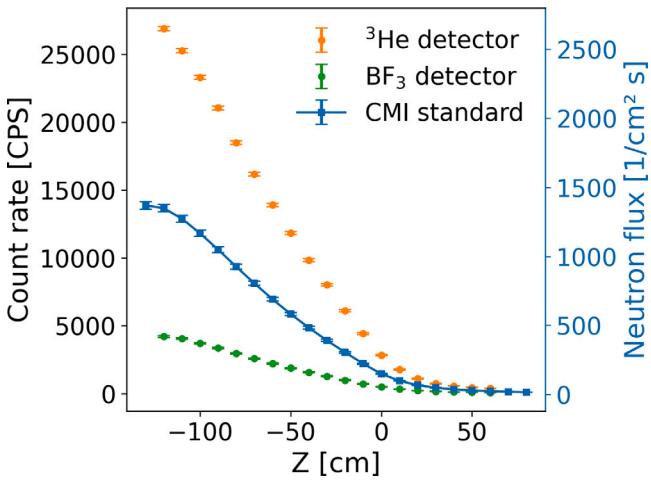

Fig. 6. Axial neutron detector signal distribution along the Z-axis in the CMI standard thermal neutron field. The blue curve shows the reference flux profile calculated with the validated MCNP model. Experimental data obtained on 13 May 2025 with the ^{3}He and BF_3 proportional counters are shown in orange and green, respectively.

The calibration was determined by correlating the reference thermal neutron fluence rate of the CMI standard field with the corresponding count rates recorded for each detector, as shown in Fig. 7. A linear relationship was observed for both detectors within their respective linear response ranges. For the ^{3}He detector, the calibration interval was restricted to the lower count rate region because of its higher

Table 2
Calibration constants obtained from the linear fits of neutron flux versus count rate measured at the CMI standard thermal neutron field.

Detector	Slope [CPS cm^2 s^1]	Uncertainty [%]
BF_3	3.28	2.5
^{3}He	16.31	5.8

detection efficiency compared to the BF_3 detector. In addition, the poorer gamma-ray discrimination of the ^{3}He detector required DAQ parameters optimised for gamma-background suppression in the KATANA measurement environment, which limited the linearity of the response at higher count rates. The slopes of the fitted lines, listed in Table 2, represent the sensitivity of each detector in terms of count rate per neutron flux. The ^{3}He detector shows higher sensitivity than the BF_3 detector.

A noticeable deviation from linearity is observed for the ^{3}He detector at high count rates, attributed to non linear effects discussed earlier, while the BF_3 detector maintains linear behaviour throughout the measured range. These calibration constants provide the necessary conversion factors for determining absolute neutron fluxes during subsequent measurements at the KATANA facility.

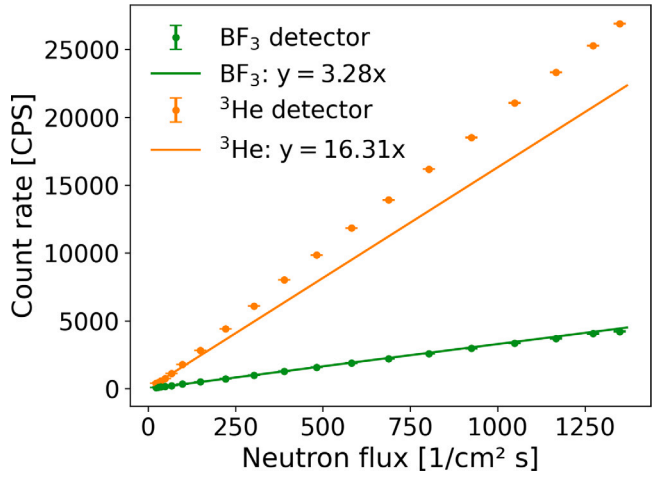

Fig. 7. Relationship between detector count rate for the ^{3}He and BF_3 proportional counters and neutron flux measured at the CMI standard thermal neutron field.

The experimental results obtained with the ^{3}He and BF_3 proportional counters are shown as orange and green markers, respectively, and include statistical uncertainty.

The calibration campaign at the CMI thermal neutron fluence standard provides response functions for both proportional counters. The following sections apply these calibration factors to measurements performed at the KATANA facility and assess detector performance under operational conditions.

4. Results

In the CMI reference neutron field and the KATANA water activation neutron field, the primary emitted neutrons are fast, i.e. up to 11 MeV for AmBe and 1.70 MeV for ^{17}N, respectively. Neutron moderation is therefore applied to slow the neutrons to the thermal energy range, where efficient detection with BF_3 and ^{3}He proportional counters is possible.

As the neutron energy distributions at the CMI reference field and the KATANA facility differ, calibration cannot rely solely on the absolute thermal neutron flux. Instead, an intermediate step consisting of Monte Carlo simulations is performed to take into account the primary neutron energy distribution and moderation to thermal energies. In the Monte Carlo simulations, reaction rates are calculated for the nuclear reactions on which the neutron detection is based (^{10}B$(n,\alpha)^7$Li, ^{3}He$(n,p)^3$H). The reaction rate is defined as

$$RR = \int \phi(E)\,\sigma(E)\,N\,\mathrm{d}E, \tag{1}$$

where $\phi(E)$ is the neutron flux as a function of energy, $\sigma(E)$ is the microscopic reaction cross section, and N is the atomic density of the target isotope in the active volume of the neutron detector [20].

The neutron detector signal is then defined as

$$RR = X \cdot CR, \tag{2}$$

where CR is the count rate recorded by the neutron detector, X is the system response factor relating the recorded count rate to the reaction rate in the detector, and RR is the reaction rate in the neutron detector. The factor X includes the combined effects of the detector response, electronics, thresholds, shaping times, pulse discrimination, and dead-time corrections. During the calibration measurements at CMI and the experimental measurements at the KATANA water activation facility, identical data-acquisition settings were used.

The calibration is formulated by using the CMI reference field to determine the detector response factor under fixed data acquisition settings, which is then applied to the KATANA measurements performed with the same detector and identical electronics settings. The reaction rates in the detector active volume for the CMI and KATANA configurations are defined as

$$RR_{\mathrm{CMI}} = \int \phi_{\mathrm{CMI}}(E)\,\sigma(E)\,N\,\mathrm{d}E, \tag{3}$$

$$RR_{\mathrm{KATANA}} = \int \phi_{\mathrm{KATANA}}(E)\,\sigma(E)\,N\,\mathrm{d}E, \tag{4}$$

where $\phi_{\mathrm{CMI}}(E)$ corresponds to the thermalised neutron spectrum resulting from the calibrated AmBe source and $\phi_{\mathrm{KATANA}}(E)$ represents the neutron flux in the detector active volume, obtained from MCNP simulations of the KATANA water activation facility, and does not correspond directly to the primary ^{17}N source spectrum.

The neutron energy spectrum in the detector active volume was obtained from MCNP simulations using an F4 track-length tally, which provides the neutron flux per source particle [10]. The absolute neutron flux is therefore given by scaling the normalised MCNP spectrum $F4(E)$ by the neutron source strength N_{SS} as

$$\phi(E) = F4(E) \cdot N_{\mathrm{SS}}. \tag{5}$$

The neutron source strength for the CMI facility ($N_{\mathrm{SS}}^{\mathrm{CMI}}$) was determined from the source characterisation and experimental measurements. By combining Eqs. (1), (2) and (5), the neutron source strength can be expressed as

$$N_{\mathrm{SS}} = \frac{CR \cdot X}{\int F4(E)\,\sigma(E)\,N\,\mathrm{d}E}. \tag{6}$$

Eq. (6) can be written separately for the CMI calibration experiment and for the KATANA measurement. Since the same detector and identical data-acquisition settings were used in both cases, the detector-response factor X determined from the CMI calibration can be substituted into the corresponding expression for the KATANA measurement. This yields the neutron source strength of the KATANA facility as

$$N_{\mathrm{SS}}^{\mathrm{KATANA}} = \frac{CR_{\mathrm{KATANA}}}{CR_{\mathrm{CMI}}} \cdot N_{\mathrm{SS}}^{\mathrm{CMI}} \cdot \frac{\int F4_{\mathrm{CMI}}(E)\,\sigma(E)\,\mathrm{d}E}{\int F4_{\mathrm{KATANA}}(E)\,\sigma(E)\,\mathrm{d}E}. \tag{7}$$

where CR_{CMI} and CR_{KATANA} are the detector count rates measured in the CMI reference field and in the KATANA facility, respectively. The atomic density of the target isotope and the active detector volume cancel because the same detector was used in both measurements. The final term represents a spectral correction factor that accounts for the different neutron energy distributions in the detector active volume in the two irradiation configurations.

Fig. 8 compares the neutron lethargy spectra of the KATANA ^{17}N field and the CMI standard field, shown together with the evaluated $^{10}B(n,\alpha)^{7}Li$ and $^{3}He(n,p)^{3}H$ cross sections from ENDF/B-VIII.0 data library [2]. The CMI spectrum is strongly thermalised. In contrast, the KATANA field includes an additional fast-neutron component extending into the MeV range, characteristic of neutrons produced by the ^{17}N decay scheme.

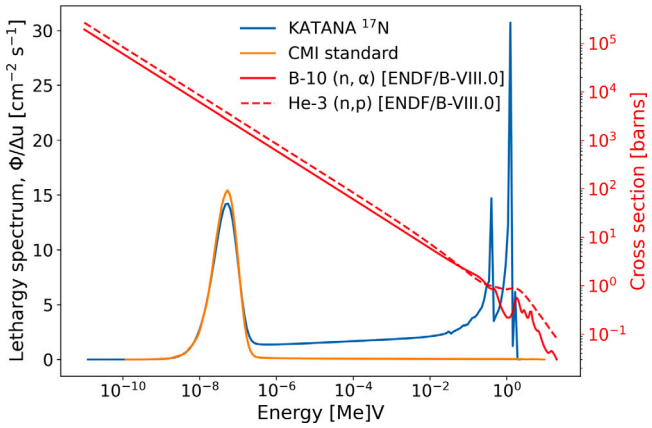

Fig. 8. Comparison of the neutron lethargy spectra of the KATANA ^{17}N field and the CMI standard field together with the evaluated $^{10}B(n,\alpha)^{7}Li$ and $^{3}He(n,p)^{3}H$ reactions cross section (ENDF/B-VIII.0).

Figs. 9 and 10 show the reaction-rate density per lethargy for the $^{10}B(n,\alpha)^{7}Li$ and $^{3}He(n,p)^{3}H$ reactions, respectively, in the CMI standard thermal neutron field and the KATANA ^{17}N neutron field. In both cases, the reaction-rate density exhibits a pronounced maximum in the thermal region around 10^{-8} MeV, which is due to the thermal neutron peak in the spectra and the characteristic $1/v$ behaviour, confirming that the dominant contribution to the total reaction rate originates from the same thermal energy range in both fields for both detector types. However, the figures also show that the neutron spectra are not identical, and these differences manifest as small but distinct variations in the reaction-rate distributions. Although these contributions remain minor relative to the thermal peak, they clearly demonstrate that the CMI and KATANA fields differ spectrally and must be taken into account.

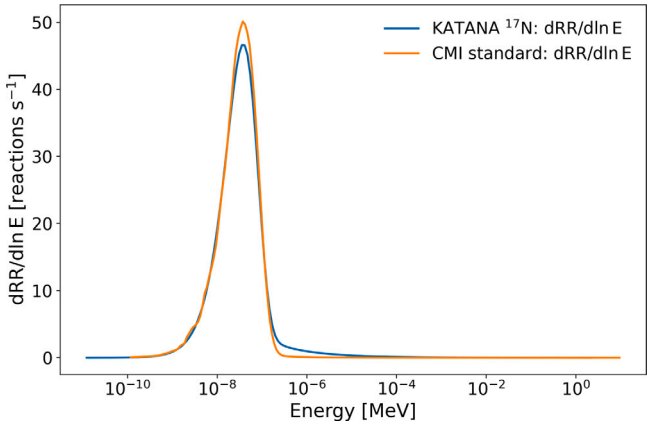

Fig. 9. Reaction rate density per lethargy, $\mathrm{dRR}/\mathrm{d}\ln E$, for the $^{10}B(n,\alpha)^{7}Li$ reaction in the CMI standard neutron field and in the KATANA ^{17}N neutron field.

The neutron source strength (N_{SS}) of the KATANA Snail No. 1 determined according to Eq. (7), using the calibration measurements and the MCNP simulations was found to be:

- $N_{SS}(250\ \mathrm{kW},\ 0.66\ \mathrm{l/s},\ \mathrm{BF_3}) = 1.7186 \cdot 10^4 (1 \pm 3.08\ \%)\ \mathrm{n/s}$,
- $N_{SS}(250\ \mathrm{kW},\ 0.66\ \mathrm{l/s},\ ^{3}\mathrm{He}) = 1.6128 \cdot 10^4 (1 \pm 6.07\ \%)\ \mathrm{n/s}$.

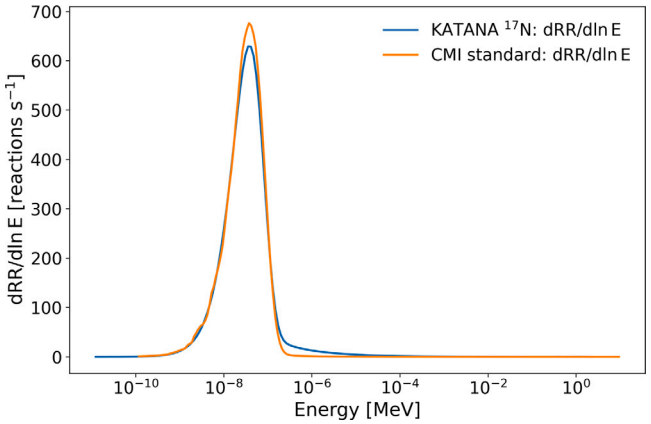

Fig. 10. Reaction rate density per lethargy, $\mathrm{dRR}/\mathrm{d}\ln E$, for the $^{3}He(n,p)^{3}H$ reaction in the CMI standard neutron field and in the KATANA ^{17}N neutron field.

This value represents the absolute source strength under JSI TRIGA steady-state operation at 250 kW thermal power and KATANA operation at a 0.66 l/s flow rate in the short loop configuration. Once the source strength was established, the validated model was used to compute neutron flux maps in absolute units, enabling direct comparison between simulated flux distributions and future measurements within the KATANA facility.

In the following results, only the flux distributions obtained from the BF_3 detector validation are presented. The corresponding analysis with the ^{3}He detector yields consistent results and confirms the same source strength and spatial flux behaviour; however, the ^{3}He measurements show larger uncertainties due to calibration. As both detectors lead to the same physical conclusions, and the BF_3 detector provides the most reliable quantitative constraints, the BF_3 based results are presented. Fig. 11 shows the absolute neutron flux distribution on a logarithmic scale, clearly visualising the spatial flux gradients. Green contour lines representing iso-flux levels are superimposed on the colour-coded flux map.

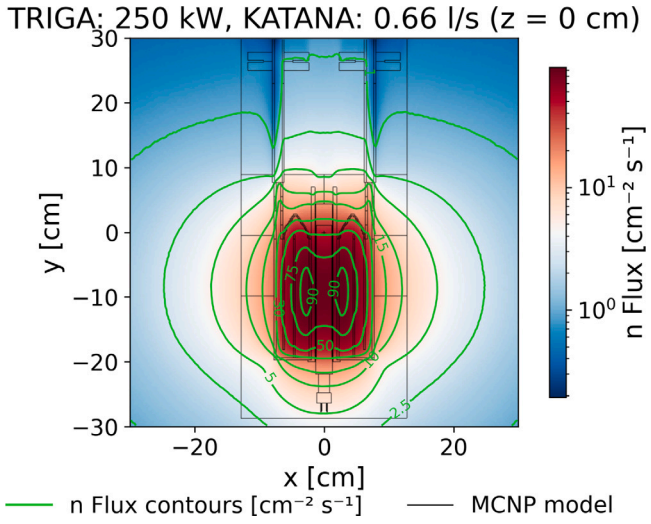

Fig. 11. Neutron flux distribution in the horizontal plane at $z = 0$ cm for the KATANA Snail No. 1 source, shown on a logarithmic scale and overlaid KATANA geometry. The flux map is overlaid with green neutron flux contours, illustrating the spatial structure and intensity gradients of the neutron field within the irradiation region.

The detector calibrations, the reaction rate-based transfer from the CMI reference field, and the MCNP simulations normalised to the

experimentally determined source strength together provide a reliable description of the neutron field within and around Snail No. 1. The resulting absolute flux distributions and their associated uncertainties constitute a characterisation of the ^{17}N induced neutron field under presented KATANA operating conditions with a uniformly distributed water activation source.

4.1. Origins of uncertainty

The total uncertainty associated with the determination of the neutron source strength and the resulting flux characterisation at the KATANA facility arises from a combination of experimental and computational contributions. The dominant experimental component originates from the detector calibration at the CMI standard neutron field, where the linear fit uncertainties of the calibration constants are 2.5% for the BF_3 detector and 5.8% for the ^3He detector. Additional contributions arise from statistical counting uncertainties during both the calibration and KATANA measurements, as well as from systematic effects such as dead-time corrections, which particularly affect the ^3He detector at elevated count rates.

In addition to these contributions, which are common to both the calibration and KATANA experimental configurations, further uncertainties are introduced by the operating conditions of the KATANA device: namely, the JSI TRIGA reactor power, which directly determines the neutron flux at the irradiation position, and the KATANA flow rate, which defines the transit time of the activated water and thus the extent of decay prior to detection. Both effects, related to power stability and flow-rate regulation, contribute to the overall measurement uncertainty [4,21]. Prior to the experiments, it was determined that the neutron background signal from reactor operation is negligible (less than 0.1 counts per second) [3].

On the modelling side, uncertainties arise from the representation of the neutron spectrum and geometry in the MCNP calculations, though these remain small (typically below one percent) owing to the validated CMI model and the well-constrained KATANA geometry. When propagated through the reaction-rate transfer, these factors yield combined relative uncertainties of 3.1% for the BF_3-based source strength and 6.1% for the ^3He-based determination. The BF_3-derived value therefore, provides the most robust normalisation of the MCNP simulations and is consequently used as the reference for the flux characterisation presented in this work.

5. Conclusions

A comprehensive calibration and validation campaign of ^3He and BF_3 proportional counters for application at the KATANA water activation facility has been conducted, combining measurements at the CMI national standard of thermal neutron fluence rate with detailed Monte Carlo modelling of the KATANA measurement volume. Calibration in the well-characterised graphite-moderated thermal neutron field at CMI provided robust detector response functions, with linear fit uncertainties of 2.5% for the BF_3 detector and 5.8% for the ^3He detector. These calibrations were transferred to the KATANA ^{17}N neutron field using a reaction-rate based calibration that accounts for the full energy dependence of the neutron spectrum and detector response, thereby ensuring consistency between the thermal reference field and the mixed neutron field produced by water activation.

The validated MCNP model of the KATANA Snail No. 1 measurement volume, derived from a detailed CAD description and incorporating the uniformly distributed ^{17}N decay source, was normalised using the experimentally determined detector response. The two independent determinations agree within their combined uncertainties, with the BF_3-based result providing the most stringent constraint on the absolute normalisation of the simulated neutron field.

The combined use of detector calibration, reaction-rate based transfer between reference and application fields, and MCNP modelling demonstrates that KATANA can deliver a well defined, ITER-relevant neutron field suitable for detector testing, shielding studies, and validation of computational tools for water activation in future fusion reactor cooling circuits. These results establish the required neutron field inputs for the subsequent evaluation of the integral $^{17}O(n,p)^{17}N$ cross section, which relies on combining the reconstructed flux with measured activation in the KATANA loop.

CRediT authorship contribution statement

Julijan Peric: Writing – review & editing, Writing – original draft, Visualization, Validation, Software, Resources, Project administration, Methodology, Investigation, Funding acquisition, Formal analysis, Data curation, Conceptualization. **Domen Kotnik:** Writing – review & editing, Writing – original draft, Supervision, Resources, Project administration, Funding acquisition. **Domen Govekar:** Writing – review & editing, Investigation. **Luka Snoj:** Writing – review & editing, Supervision, Project administration, Funding acquisition, Conceptualization. **Zdenek Vykydal:** Resources, Investigation, Formal analysis, Data curation. **Marco De Pietri:** Writing – review & editing, Validation. **Vladimir Radulović:** Writing – review & editing, Validation, Supervision, Project administration, Funding acquisition, Formal analysis, Conceptualization.

Declaration of competing interest

The authors declare that they have no known competing financial interests or personal relationships that could have appeared to influence the work reported in this paper.

Acknowledgements

The authors acknowledge the support of the Slovenian Research and Innovation Agency (project codes P2-0405 Fusion technologies; P2–0073 Reactor physics; PR-12326/ PR-12842 Training of young researchers, NC-0022 Water activation in nuclear reactors). This work has been carried out within the framework of the EUROfusion Consortium, funded by the European Union via the Euratom Research and Training Programme (Grant Agreement No 101052200 — EUROfusion). Views and opinions expressed are however those of the author(s) only and do not necessarily reflect those of the European Union or the European Commission. Neither the European Union nor the European Commission can be held responsible for them.

Data availability

Data will be made available on request.

References

[1] A. Žohar, I. Lengar, L. Snoj, Analysis of water activation in fusion and fission nuclear facilities, Fusion Eng. Des. 160 (2020) 111828, http://dx.doi.org/10.1016/j.fusengdes.2020.111828.

[2] D. Brown, M. Chadwick, R. Capote, A. Kahler, A. Trkov, M. Herman, A. Sonzogni, Y. Danon, A. Carlson, M. Dunn, D. Smith, G. Hale, G. Arbanas, R. Arcilla, C. Bates, B. Beck, B. Becker, F. Brown, R. Casperson, J. Conlin, D. Cullen, M.-A. Descalle, R. Firestone, T. Gaines, K. Guber, A. Hawari, J. Holmes, T. Johnson, T. Kawano, B. Kiedrowski, A. Koning, S. Kopecky, L. Leal, J. Lestone, C. Lubitz, J. Márquez Damián, C. Mattoon, E. McCutchan, S. Mughabghab, P. Navratil, D. Neudecker, G. Nobre, G. Noguere, M. Paris, M. Pigni, A. Plompen, B. Pritychenko, V. Pronyaev, D. Roubtsov, D. Rochman, P. Romano, P. Schillebeeckx, S. Simakov, M. Sin, I. Sirakov, B. Sleaford, V. Sobes, E. Soukhovitskii, I. Stetcu, P. Talou, I. Thompson, S. van der Marck, L. Welser-Sherrill, D. Wiarda, M. White, J. Wormald, R. Wright, M. Zerkle, G. Žerovnik, Y. Zhu, ENDF/B-VIII.0: The 8th major release of the nuclear reaction data library with CIELO-project cross sections, new standards and thermal scattering data, Nucl. Data Sheets 148 (2018) 1–142, http://dx.doi.org/10.1016/j.nds.2018.02.001, Special Issue on Nuclear Reaction Data.

[3] J. Peric, D. Kotnik, L. Snoj, V. Radulović, Neutron emission from water activation: Experiments and modeling under fusion-relevant conditions at the KATANA facility, Fusion Eng. Des. 216 (2025) 115052, http://dx.doi.org/10.1016/j.fusengdes.2025.115052.
[4] D. Kotnik, J. Peric, D. Govekar, L. Snoj, I. Lengar, KATANA - water activation facility at JSI TRIGA, Part I: Final design and activity calculations, Nucl. Eng. Technol. (2024) http://dx.doi.org/10.1016/j.net.2024.09.036.
[5] L. Snoj, et al., A half-century of nuclear research, education and training: Story of the JSI TRIGA reactor, Ann. Nucl. Energy 214 (2025) 111122, http://dx.doi.org/10.1016/j.anucene.2024.111122.
[6] ITER organization, "ITER homepage", 2024, http://www.iter.org. (Accessed: 02 May 2024).
[7] X. Litaudon, U. Fantz, R. Villari, V. Toigo, M.-H. Aumeunier, J.-L. Autran, P. Batistoni, E. Belonohy, S. Bradnam, M. Cecchetto, A. Colangeli, F. Dacquait, S.D. Bello, M. Dentan, M.D. Pietri, J. Eriksson, M. Fabbri, G. Falchetto, L. Figini, J. Figueiredo, D. Flammini, N. Fonnesu, L. Frassinetti, J. Galdón-Quiroga, R. Garcia-Alia, M. Garcia-Munoz, Z. Ghani, J. Gonzalez-Martin, E. Grelier, L. Di Grazia, B. Grove, C. Grove, A. Gusarov, B. Heinemann, A. Hjalmarsson, O. Hyvärinen, V. Ioannou-Sougleridis, L. Jones, H.-T. Kim, M.K. osowski, M. Kocan, B. Kos, L. Kos, D. Kotnik, E. Laszynska, D. Leichtle, I. Lengar, E. Leon-Gutierrez, A. López-Revelles, S. Loreti, M. Loughlin, D. Marcuzzi, K. Mcclements, G. Mariano, M. Mattei, K. Mergia, J. Mietelski, R. Mitteau, S. Moindjie, D. Munteanu, R. Naish, S. Noce, L. Packer, S. Pamela, R. Pampin, A. Pau, A. Peacock, E. Peluso, Y. Peneliau, J. Peric, V. Radulović, D. Ricci, F. Rimini, L. Sanchis-Sanchez, P. Sauvan, M. Savva, G. Serianni, C. Shand, A. Snicker, L. Snoj, I. Stamatelatos, Z. Štancar, N. Terranova, T. Vasilopoulou, R. Vila, J. Waterhouse, C. Wimmer, D. Wünderlich, A. Žohar, the NBTF Team and JET Contributors, the EUROfusion Tokamak Exploitation Team, EUROfusion contributions to ITER nuclear operation, Nucl. Fusion 64 (11) (2024) 112006, http://dx.doi.org/10.1088/1741-4326/ad346e.
[8] D. Kotnik, J. Peric, D. Govekar, L. Snoj, I. Lengar, KATANA - water activation facility at JSI TRIGA, Part II: First experiments, Nucl. Eng. Technol. (2024) http://dx.doi.org/10.1016/j.net.2024.10.052.
[9] D. Kotnik, A.K. Basavaraj, L. Snoj, I. Lengar, Design optimization of the closed-water activation loop at the JSI irradiation facility, Fusion Eng. Des. 193 (2023) 113632, http://dx.doi.org/10.1016/j.fusengdes.2023.113632.
[10] J.A. Kulesza, T.R. Adams, J.C. Armstrong, S.R. Bolding, F.B. Brown, J.S. Bull, T.P. Burke, A.R. Clark, R.A. Forster III, J.F. Giron, A.S. Grieve, C.J. Josey, R.L. Martz, G.W. McKinney, E.J. Pearson, M.E. Rising, C.J. Solomon Jr., S. Swaminarayan, T.J. Trahan, C.A. Weaver, S.C. Wilson, A.J. Zukaitis, MCNP® Code Version 6.3.1 Theory & User Manual, Tech. Rep. LA-UR-24-24602, Rev. 1, Los Alamos National Laboratory, Los Alamos, NM, USA, 2024, http://dx.doi.org/10.2172/2372634.
[11] J. Catalán, P. Sauvan, J. García, J. Alguacil, F. Ogando, J. Sanz, GEOUNED: A new conversion tool from CAD to Monte Carlo geometry, Nucl. Eng. Technol. 56 (6) (2024) 2404–2411, http://dx.doi.org/10.1016/j.net.2024.01.052.
[12] International Atomic Energy Agency, Guidelines on Calibration of Neutron Measuring Devices, Tech. Rep. 285 IAEA Technical Reports Series, International Atomic Energy Agency, Vienna, 1988, STI/DOC/10/285.
[13] X. Campo, R. Méndez, S. Rivera, F. González, Analysis of the standard calibration methods for neutron monitors, Radiat. Phys. Chem. 222 (2024) 111844, http://dx.doi.org/10.1016/j.radphyschem.2024.111844.
[14] Z. Vykydal, M. Králík, A. Jančář, Z. Kopecký, J. Dressler, M. Veškrna, Characterization of the graphite pile as a source of thermal neutrons, Radiat. Phys. Chem. 116 (2015) 65–68, http://dx.doi.org/10.1016/j.radphyschem.2015.01.028, Proceedings of the 9th International Topical Meeting on Industrial Radiation and Radioisotope Measurement Applications.
[15] Z. Vykydal, M. Králík, Characterisation of the graphite moderated thermal neutron field at CMI, Radiat. Prot. Dosim. 180 (1–4) (2017) 51–55, http://dx.doi.org/10.1093/rpd/ncx190.
[16] J. Rusnak, Z. Vykydal, Determination of a Pu-Be source neutron spectrum at Czech Metrology Institute, Appl. Radiat. Isot. 175 (2021) 109786, http://dx.doi.org/10.1016/j.apradiso.2021.109786.
[17] International Atomic Energy Agency, Neutron Fluence Measurements, Tech. Rep. 107 IAEA Technical Reports Series, International Atomic Energy Agency, Vienna, 1970, STI/DOC/10/107.
[18] P. Rubovič, D. Ekendahl, Z. Vykydal, J.H. ulka, B. Bergmann, S. Pospíšil, I. Štekl, Dosimetry in mixed neutron-gamma fields with a Timepix detector, Radiat. Meas. 119 (2018) 22–26, http://dx.doi.org/10.1016/j.radmeas.2018.08.018.
[19] P. Smolyanskiy, M. Bacak, B. Bergmann, P. Broulím, P. Burian, T. Čelko, D. Garvey, K. Gunthoti, F. Infantes, P. Mánek, A. Manna, F. Mráz, R. Mucciola, S. Pospíšil, M. Sitarz, O. Urban, Z. Vykydal, S. Wender, A two-layer Timepix3 stack for improved charged particle tracking and radiation field decomposition, J. Instrum. 19 (02) (2024) C02016, http://dx.doi.org/10.1088/1748-0221/19/02/C02016.
[20] J. Lamarsh, A. Baratta, Introduction to Nuclear Engineering, in: Addison-Wesley series in nuclear science and engineering, Pearson Prentice Hall, 2011.
[21] Z. Stancar, L. Snoj, An improved thermal power calibration method at the TRIGA Mark II research reactor, Nucl. Eng. Des. 325 (2017) 78–89, http://dx.doi.org/10.1016/j.nucengdes.2017.10.007.